Thermal Modeling and Adaptive Control of Scan Welding

A numerical simulation and a thermal control strategy are used to implement scan welding on a robotic PAW station

BY C. C. DOUMANIDIS

ABSTRACT. This article introduces scan welding as a redesign of classical joining methods, employing automation technology to ensure the overall geometric, material and mechanical integrity of the joint. This is obtained by real-time control of the welding temperature field by a proper dynamic heat input distribution on the weld surface. This distribution is implemented in scan welding by a single torch, sweeping the joint surface by a controlled reciprocating motion, and power adjusted by feedback of infrared temperature measurements in-process. An off-line numerical simulation of the thermal field in scan welding is established, as well as a linearized multivariable model with real-time parameter identification. An adaptive thermal control scheme is thus implemented and validated — both computationally and experimentally on a robotic plasma arc welding (PAW) station. The resulting thermal features related to the generated material structure and properties of the joint are finally analyzed in scan welding tests and simulations.

Introduction

Since the early days (circa 1880) of Benardos, the inventor of electric welding, one can hardly overestimate the impact of multifaceted welding methods upon modern manufacturing. Commensurate with its ubiquitous applications has been the progress of welding operations technology itself: The carbon electrode arcs of Benardos have been replaced by powerful gas tungsten and gas metal arc, plasma, laser or electron beam sources. The manual skills (*i.e.*, the senses and judgment of the human operator to whom joining tasks were historically entrusted) have gradually been replaced by automated systems, dictated by improved economics and production rates. Welding automation hinges on the development of numerous technologies such as the following:

- Actuators such as mechanized positioners and flexible robots to substitute human labor in harsh welding environments.
- Advanced sensors such as optical, acoustic and ultrasonic detectors to monitor various process conditions (including variables unobservable by humans).
- Computer technology to implement intelligence and control functions of the technician to ensure reliable and improved welding operations.

Automation in welding technology — both in off-line analysis and real-time control of the process — not only has assisted in improving the performance of classical methods, but also has led to the development of alternative welding techniques (Ref. 1). These operations must be designed to optimize the product in its totality, including weld bead geometry, material structure in the heat-affected zone (HAZ) and mechanical properties of the joint. The combination of desirable weld characteristics in all these aspects is imperative. A weld may have an ideal bead geometry, but suffer from a martensitic structure in steels, an overaged θ-phase in precipitation-hardened aluminum alloys, a sensitization zone in stainless steels (Ref. 2) or extensive residual stresses (Ref. 3) rendering the weldment useless — as the fate of the Liberty ships in World War II has demonstrated (Ref. 4). Bead morphology, metallurgical microstructure and thermal stress or distortion fields are all time-dependent, spatially distributed features; therefore, they may not simultaneously be controllable by the few lumped process variables of localized, sequentially moving heat sources such as a plasma arc or a laser beam (Ref. 1). A distributed, simultaneous heat input on the entire accessible weld surface may be desirable to regulate the bead profile, microstructure and property distributions in the joint volume. One solution to expand the control authority of concentrated heat sources that has been tried in the literature (Refs. 5–6–7) involves multiple torches distributed in space. However, such hardware arrangements are plagued by the complexity and cost of multiple power sources and by resolution and interference problems among torches.

KEY WORDS

Adaptive Control
Infrared Pyrometry
Scan Welding
Thermal Model

Objectives

An alternative software approach, in which a single-point heat source is shared in time to generate the necessary heat input distribution for thermal control of the weld, is enabled by automation technology in the scan welding technique (Ref. 8). A traditional welding torch or beam, guided by a high-speed servosystem or robotic manipulator, sweeps rapidly across the full part surface. This provides the right amount of thermal power at each surface element, which is needed to develop a specified local temperature cycle and thus the desirable ther-

C. C. DOUMANIDIS is with the Department of Mechanical Engineering, Tufts University, Medford, Mass.

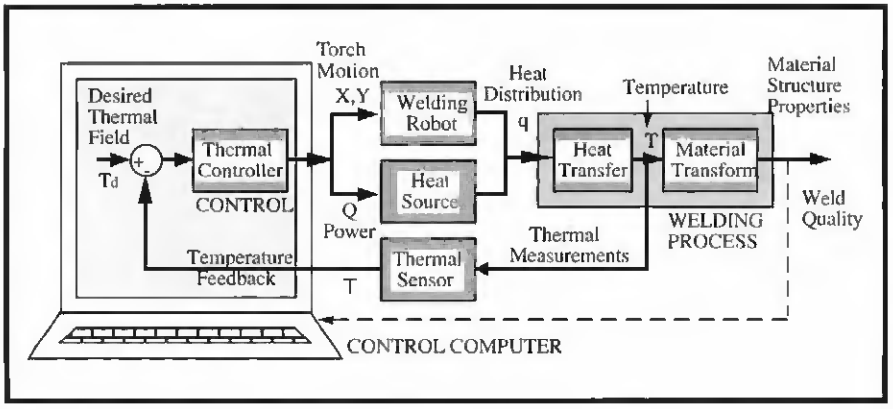

Fig. 1 — Schematic arrangement of closed-loop thermal control in welding.

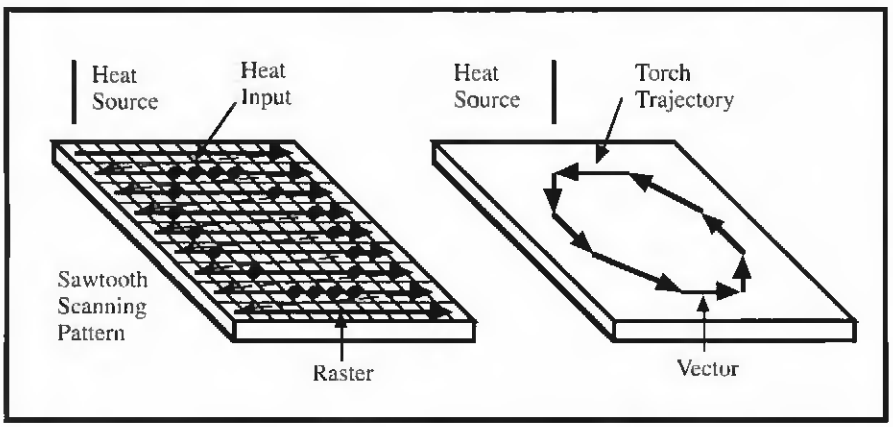

Fig. 2 — Raster and vector thermal scanning of an octagonal welding pattern.

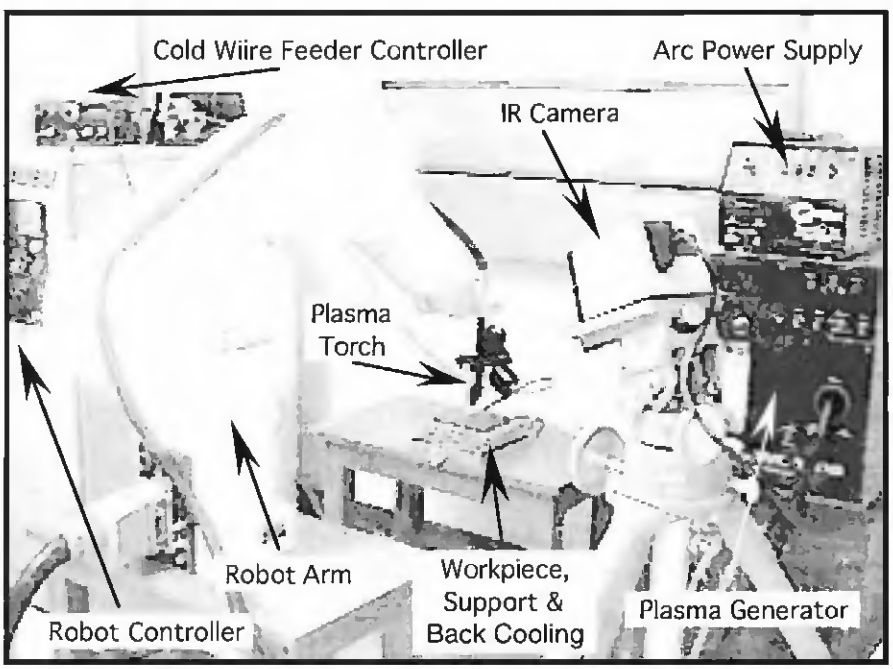

Fig. 3 — Laboratory setup of robotic plasma-arc scan welding station.

mal distributions in the weld. The heat-source power and trajectory are dynamically modulated in real time by the control computer, using feedback of thermal measurements on the joint by a noncontact sensor. However, such technology of nondestructive, in-process sensing of internal material characteristics (*e.g.*, ultrasonic or X-ray imaging) is currently costly and impractical. It also involves long time delays in measuring features such as residual stresses that are finalized as the part cools down after the process is completed. Fortunately, these characteristics are determined by the dynamic temperature field during the operation, which can readily be measured on the external surface, e.g., by non-invasive infrared pyrometry (Ref. 9) — Fig. 1.

Thus, scan welding can be visualized as a computer-controlled, two-dimensional weaving of a point heat source with thermal feedback, capable of generating a desirable distribution of the preheating, welding and/or postheating cycle in the processed joint. The experimental testing and parametric analysis of the scan welding technique — both for planar, orthogonal metal sheets and circular flange and pipe arrangements — has been reported in the literature (Ref. 10). The off-line thermal modeling and real-time adaptive control of the process conditions (*i.e.*, the source power and motion of the scan welding method) are the objectives of this article. After a description of a computational simulation of the temperature field in scan welding, an in-process thermal regulation strategy is established and implemented by the thermal controller of the scan welding configuration in the laboratory.

Experimental Implementation

The thermal actuation in scan welding can be implemented in two different modes. High-bandwidth sources such as electron beam welding (EBW) or laser beam welding (LBW) can be scanned in a raster pattern on the weld surface in a sawtooth (row-wise) fashion (similar to the beam scanning in a CRT monitor), while their intensity is simultaneously modulated for each raster element (pixel) — Fig. 2. For slow-moving sources such as arc or plasma-arc torches, a more efficient actuation is obtained by vector scanning of the heat source on a real-time guided trajectory, similar to the beam scanning on an oscilloscope screen — Fig. 2. In this case, a mechanical two-degrees-of-freedom positioning system of the torch relative to the part is needed (*e.g.*, a servo-driven X-Y table or a robotic manipulator).

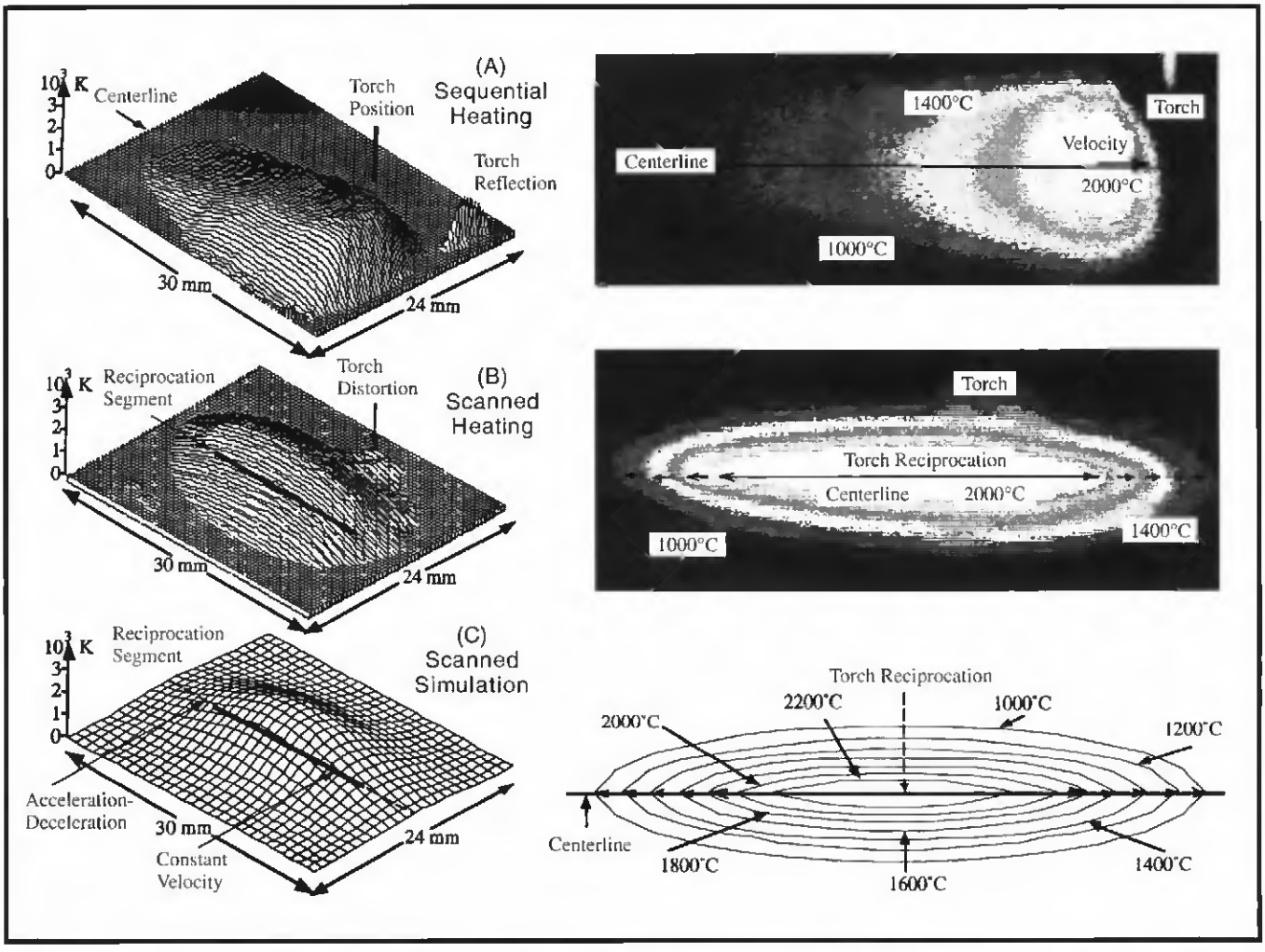

Fig. 4 — Temperature hills and isotherm contours on top surface of open-loop traditional and scan welding. A — Classical welding; B — scan welding; C — numerical simulation of scan welding.

Such a vector-scanning technique is implemented on the experimental scan-welding station as shown in Fig. 3. It consists of a water-cooled PAW torch, rated at 300 A and powered by a multifunction CC/CV transformer supply rated at 400 A, through a plasma console unit and a closed-circuit coolant recirculator. The PAW system is capable of both transferred plasma arc for metals and non-transferred (pilot) plasma arc mode for metals and nonmetallic materials. In the experiments, which consist of autogenous bead-on-plate scan welding of stainless steel (304) coupons measuring 30 x 24 x 3 mm, the arc voltage is 15 V, the torch height (elevation) is 3 mm, and the plasma and shielding gas (Ar-2%O_2) flow is 0.5 L/s. The PAW torch is guided by an articulated six-degrees-of-freedom process robot, with a positioning accuracy of 0.15 mm, maximum speed of about 1 m/s and payload of up to 6 kg. The manipulator is powered by AC servomotors with optical encoder feedback hardened for high-frequency arc initiation interference in welding, and its control unit is programmable in high-level code through an embedded terminal and teach pendant. The frequency of reciprocation of the robotically guided torch can be selected by the user in open-loop scan welding and is governed by the thermal controller in closed-loop operation. The robot controller, as well as the PAW supply, are connected to the central microcomputer of the setup through a serial and AD/DA converter board respectively, ensuring software control of the torch motion and power in real time.

The same system computer is used to monitor the temperature field on the top surface of the weld by a stationary infrared pyrometry camera. This consists of a high-speed, 2-D, electro-mechanical galvanometer scanner, a set of focusing lenses and filters and a liquid nitrogen-cooled HgCdTe sensor element that is sensitive in the 8–12 μm wavelength range. The temperature resolution of the infrared camera is ±2 K on a 1000-K window range, and the spatial resolution of the scanner is 0.2 mrad, equivalent to about 0.2 mm on the weld surface. A microprocessor-based control unit converts the measured infrared emission values to temperatures based on user-defined surface emissivity values. The surface emissivity is calibrated by comparison of the infrared data to the measurements of K-type thermocouples. The dynamic thermal image, besides being monitored in-process by the control computer through a high-performance frame grabber, is also stored in standard composite video format by a tape recorder for off-line thermal analysis by dedicated image processing software. This analysis yields the temperature hill on the top surface of the weldment, as well as the isotherm contours, *i.e.*, sections of the temperature hill at various specified temperatures.

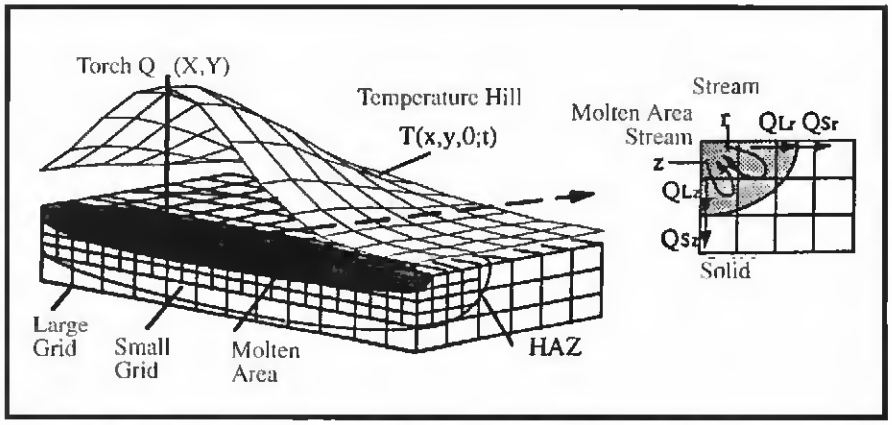

Fig. 5 — Geometric arrangement of numerical simulation for scan welding in the solid and molten region.

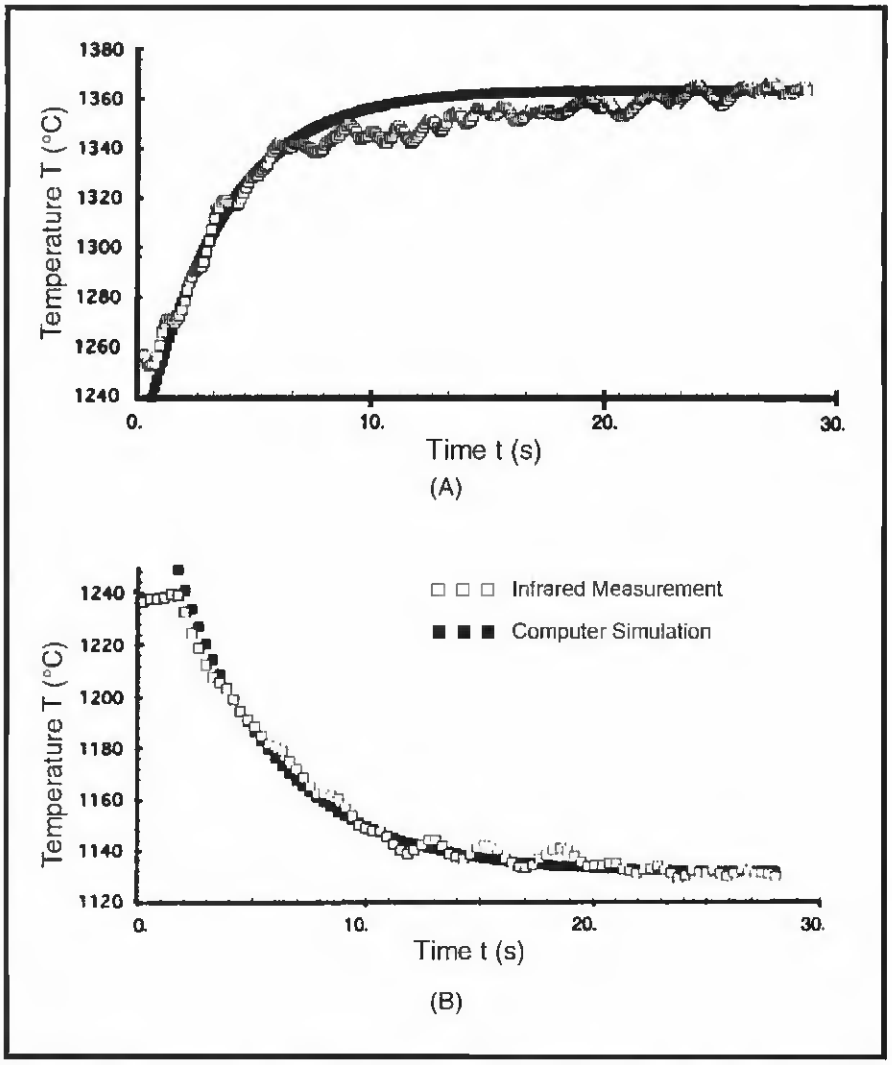

Fig. 6 — Temperature transients in scan welding at a surface point 6 mm off the centerline. A — Power step from 80 to 90 A; B — power step from 80 to 70 A.

Figure 4A and B illustrate typical infrared images of the isotherms and temperature hills on the top weld surface — generated by traditional welding at an arc current of 80 A and speed of 2 mm/s — and by scan welding at a reciprocation frequency of 2 Hz along the coupon centerline, respectively. For this scanned torch motion, the isotherms including the weld pool contours (the solidus isotherm T_s) appear elongated along the weld axis in comparison to those generated by the conventional method. As expected, unlike the concentrated temperature hill of classical welding, the scanned process yields a more uniform thermal distribution along the joint. At the two plate ends (near the robot deceleration/acceleration region of the scanned torch path) smearing of the temperature hill yields ellipsoidal thermal isotherm endings. Note also the apparent local distortion of the thermal field at the torch location and its reflection on the weld surface. The noise of the experimental data is attributed to emissivity variations of the weld surface.

Thermal Modeling

Besides laboratory experimentation, computer simulation of scan welding is necessary for the design of a thermal control system for manufacturing applications. This is because the variety of heat transfer phenomena in welding must be repeatably and accurately reproduced and studied over the full range of their important parameters, without laboratory constraints and uncertainty. Also, computational simulation overcomes the difficulty or inability of nonintrusive measurements of certain features, such as internal temperatures, weld penetration geometry, material structure and properties and stress distribution during the process. These reasons have historically contributed to the proliferation of such models since the days of analog computers, when the thermal distribution in welding was simulated by physical analogy to electrical charge dissipation in carbon specimens (Ref. 11). However, despite the wealth of welding literature in empirical (Refs. 12, 13), analytical (Refs. 14, 15) and numerical models (Refs. 16, 17) of classical welding methods, there is no direct modeling precedent for the new scan welding technique.

Model Description

Thus, a numerical finite-difference simulation of the temperature and solid-liquid phase field was developed as an off-line process description. This integrates the transient solid conduction (Fourier) equation in discrete time steps *dt* and space elements *ds* of a grid of nodes (Fig. 5), using an Eulerian formulation:

$$T(x,y,z;\ t+dt)=T(x,y,z;\ t)+\frac{\alpha.dt}{ds^2}$$
$$\sum_{\pm}\Big(\gamma_x\big(T(x\pm ds,y,z;\ t)-T(x,y,z;\ t)\big)$$
$$+\gamma_y\big(T(x,y\pm ds,z;\ t)-T(x,y,z;\ t)\big)$$
$$+\gamma_z\big(T(x,y,z\pm ds;\ t)-T(x,y,z;\ t)\big)\Big)$$
$$-\left\{\frac{2\alpha.dt}{\lambda.ds}\Big(a.\big(T(x,y,0;\ t)-T_a\big)\right.$$
$$+\varepsilon\sigma\big(T^4(x,y,0;\ t)-T_a^4\big)$$
$$\left.-q(x,y,0;\ t)\Big)\right\} \qquad (1)$$

where T is the temperature of a grid node (x,y,z) at time t. $\alpha = \lambda/\rho c$ is the thermal diffusivity, λ the conductivity, ρ the density and c the specific heat capacity of the material. The directional conduction factors take the value $\gamma_x = \gamma_y = \gamma_z = 1$ in the solid region. The last term of Equation 1 (in brackets) applies only to nodes on the weld surfaces, and represents the heat losses by convection and radiation, as well as the heat input from the torch, respectively. T_a is the temperature of the welding environment, a is the convection coefficient to the inert gas flow, ε the total hemispherical emissivity of the object surface and σ Stefan's constant. q is the thermal power influx from the heat source, modeled according to a normal (Gaussian) radial power density distribution on the part surface (Ref. 15):

$$q(x,y,0;\ t)=\frac{f.Q(t)}{ds^2}\exp\left(-\frac{(x-X(t))^2+(y-Y(t))^2}{2s^2}\right) \qquad (2)$$

where Q is the power of the torch located at position (X,Y), f its thermal efficiency and s the deviation radius of its intensity distribution. f and s are calibrated by laboratory tests so that the numerical model matches the size of the measured weld bead cross section (Ref. 18).

In the molten region, heat dissipation is influenced by natural convection (buoyancy), inert gas shear, surface tension (Marangoni effect), electromagnetic stirring (Lorentz effect) and viscous friction to the solid boundary — all giving rise to melt circulation. Figure 5 displays a generic two-stream flow pattern on a cross section of the molten pool that has been observed experimentally (Ref. 19). In the computer simulation, the circulation of the melt is accounted for by equivalent anisotropic conduction through the directional conduction factors gx, gy, gz in the three directions. These parameters in the weld pool are identified by an embedded lumped model of the melt flow (Ref. 18). In the longitudinally uniform scanning configuration of Fig. 5, for example, the two-dimensional melt circulation at the cross section of the uniform weld pool yields the values

$$\gamma_x \approx 1,\ \gamma_y=\frac{\alpha\left(\rho H\dot{w}+Q_{Sr}\right)}{\alpha' Q_{Lr}},$$
$$\gamma_z=\frac{\alpha\left(\rho H\dot{d}+Q_{Sz}\right)}{\alpha' Q_{Lz}} \qquad (3)$$

where α' is the thermal diffusivity of the melt, H the latent heat of fusion/solidification, $\dot{w}$ and $\dot{d}$ the rates of change of the width and depth of the weld pool, respectively, computed by the lumped-melt circulation model. Q_L and Q_S are the heat flux components from the liquid (subscript L) to the solid (subscript S) side of the molten pool interface, in the lateral (subscript r) and vertical (subscript z) direction, respectively.

The numerical simulation employs a large, coarse grid of nodes encompassing the full HAZ of the part and a small, finer grid for better resolution in the vicinity of the molten region — Fig. 5. These grids can be stationary, spanning the full part size, or relocatable, following the torch motion. The simulation code covers various basic process arrangements, such as planar sheets and cylindrical welds, and is easily expandable to more general geometry configurations. The reinforcement geometry resulting for filler material addition is also handled by progressive activation of the respective grid nodes on overlaying layers of the grids, to simulate material deposition. The simulation can handle heat sources with arbitrary power density distributions and trajectories in traditional and scan welding arrangements. The numerical model provides for flexible initial preheat and boundary heat transfer conditions and temperature-dependent material properties with latent transformation effects, such as fusion and solidification. The simulation output includes maps of the 3-D thermal and solid-liquid phase fields, as well as 2-D temperature hill and isotherm surface sections. A flow diagram of this computational simulation is illustrated on the right side of Fig. 10.

Model Validation

Figure 4C compares the top surface isotherm contours and temperature hill developed during scan welding, as predicted by the numerical simulation, to the measurements of the infrared camera in Fig. 4B, under the same process conditions as in the previous section. Clearly, despite certain deviations near the solid-melt interface and the plate edges because of uncertainty in the assumed material and heat transfer parameters, the thermal data in the laboratory confirm the results of the simulation model. In addition, Fig. 6 compares the dynamic time transients of the experimentally-sensed to the computationally predicted temperature at a location 6 mm off the coupon centerline on its middle section (at the side of the torch center) during a step change of the torch power in scan welding. In particular, in Fig. 6A the nominal arc current of 80 A is suddenly increased to 90 A, while in Fig. 6B it is decreased to 70 A. Again, the simulated thermal responses are in good correspondence to the measured ones, with the exception of the emissivity-related noise of the latter and a small-amplitude oscillation due to synchronization of the sampled data to the torch reciprocation. It can be seen in this figure that, although the scanning technique improves the speed of the welding dynamics, it does not eliminate the thermal lag between the power change and the resulting temperature response.

Model Use

Thermal Parameter Identification

The quantitative gray-scale infrared images and the simulated temperature distributions of Fig. 4 and the thermal responses in Fig. 6 demonstrate the continuous-time, spatially distributed nature of heat transfer in scan welding. However, for such an infinite-dimensional formulation of the scan welding model, distributed-parameter systems theory has not yet yielded practical controller design tools applicable to thermal manufacturing problems (Ref. 20). In addition, the off-line numerical simulation above cannot offer a computationally efficient basis for thermal process control in real time. A succinct alternative description, which can serve as an in-process reference model to the control algorithm, must be established through lumping of the continuous thermal distribution to vectors of distinct temperature outputs $\underline{T}$ and heat inputs $\underline{Q}$ at the nodes of a mesh of element size Ds in the weld, which are updated periodically every sampling period Dt. Such a discrete-time, finite-dimensional modeling approach is illustrated in the two-dimensional thermal distribution on the thin metal sheet of Fig. 7, in which the temperature is assumed uniform in the thickness direction. On such an orthogonal mesh of dimen-

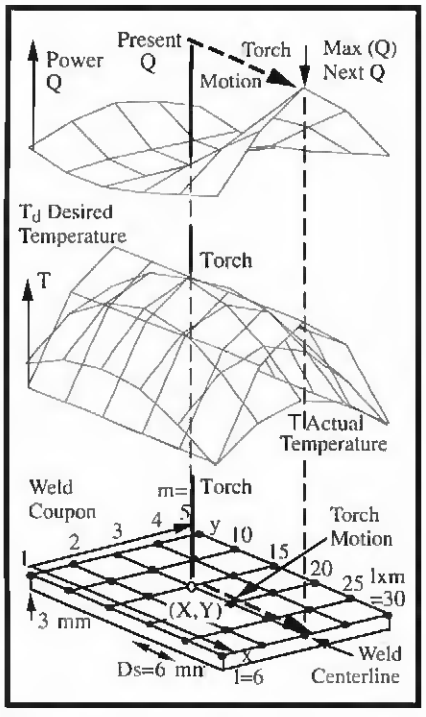

Fig. 7 — Linearized thermal model with mesh of input/output nodes on surface, actual T and desired temperature hill T_d, and heat source distribution Q.

sions $l \times m = N$ ($l = 6$, $m = 5$ in Fig. 7), the localized, sampled values of temperatures $T(i; k)$ and heat inputs $Q(i; k)$ in vectors $\underline{T}(k)$ and $\underline{Q}(k)$ respectively, are defined at each node $i = 1 \ldots N$ and time instant k. By linearization of the heat transfer Equation 1, the multivariable dependence of the resulting temperature outputs $\underline{T}(k+1)$ at the next sampling period on the current heat inputs $\underline{Q}(k)$ can be expressed in a discrete-time, autoregressive moving average (ARMA) form (Ref. 21) as follows:

$$\underline{T}(k+1) = \Theta^T(k) \cdot \underline{S}(k) \qquad (4)$$

where the augmented thermal vector $\underline{S}$ contains the present and a number n of past values of the lumped temperatures $\underline{T}$ and heat inputs $\underline{Q}$, assembled in a single column:

$$\underline{S}(k) = \left[\underline{T}^T(k):\underline{T}^T(k-1):\ldots:\underline{T}^T(k-n):\right.$$
$$\left.\underline{Q}^T(k):\underline{Q}^T(k-1):\ldots:\underline{Q}^T(k-n)\right]^T \qquad (5)$$

The parameters in matrix Θ in the linearized, multiple-input, multiple-output (MIMO) formulation of Equation 4 express the thermal dependence of each local, instantaneous temperature $T(i;$ $k+1)$ at node i and period $k+1$, on the temperature $T(j; h)$ or heat input $Q(j; h)$ at another node j and past period $h = k \ldots k-n$. The values of the independent parameters in matrix Θ can be conveniently estimated by the numerical simulation of scan welding at a thermal equilibrium corresponding to nominal conditions $\underline{T}_d$, $\underline{Q}_d$ of linearization for Equation 4, through unit perturbations of the temperatures and heat inputs at the respective locations. Thus, the temperature changes $T(i;\ k+1)$ computed at various nodes i and sampling periods k, after the temperature $T(j; h)$ or heat input $Q(j; h)$ at node j is perturbed by 1 *K* or 1 *J* respectively, reflect the related parameters in Θ.

As shown in Equation 1, however, scan welding involves nonlinearities and time variations of heat transfer mechanisms. These include radiation effects, thermal drift of the temperature-dependent material properties (especially in the presence of structural transformations with latent phenomena, e.g., fusion and solidification), and alterations of the torch characteristics and part geometry. These effects yield time-dependent dynamic parameters $\Theta(k)$ in the linearized model of Equation 4, during the thermal transients or process disturbances from the operating conditions. Thus, the initial off-line estimates of the essential time-varying parameters in Θ must be updated in-process, using temperature measurements $\underline{T}$ for the applied heat inputs $\underline{Q}$. Such a real-time parameter identification is performed by a recursive adaptation law, based on a least-squares identification method (Ref. 21). In particular, if the temperature data $\underline{T}$ and known heat values $\underline{Q}$ are substituted in Equation 4, this must in principle be solved for the thermal parameters in Θ:

$$\underline{T}(k+1) = \Theta^T(k) \cdot \underline{S}(k) \Leftarrow \text{solve for } \Theta(k) \qquad (6)$$

However, since in general the number of unknown independent elements in Θ is different than the number of scalar linear relations in Equation 6, a least-squares technique is invoked to determine the optimal combination of parameters in Θ. This selection minimizes a quadratic index of the thermal errors, *i.e.*, the deviations of the measured temperatures $\underline{T}$ from the model predictions $\underline{T}$ of Equation 4.

Temperature Reference Specification

As explained in the introduction, the overall quality of scan weldments must be regulated through real-time control of the dynamic thermal field $\underline{T}$ to a specified temperature distribution $\underline{T}_d$ (Fig. 1), dictated by the desired metallurgical and thermomechanical characteristics of the joint. In general, these material specifications can be expressed in terms of three types of thermal entities: isotherms, cooling cycles and temperature gradients. The geometry of isotherm boundaries in the weld can be specified to set the extent of both the weld bead and the HAZ. Thus, to ensure a sufficient molten-zone size along the weld centerline, the necessary contours of the solidus isotherm, *i.e.*, the solid-liquid interface, must be prescribed. Such a specification should be conservative because of the potential for solidification defects — porosity, inclusions, unfused areas and shrinkage cracks — in the weld bead. Isotherm size constraints are also appropriate in the HAZ, when thermodynamically induced (isothermal or equilibrium) metallurgical transformations take place (Ref. 3). Examples include recovery, recrystallization or grain-coarsening zones, areas of undesirable phases, such as the sensitization region of stainless steels or the overaging zone of precipitation-hardened aluminum alloys, and areas contaminated from the welding environment or the diluted pool. Cooling cycles, on the other hand, must be specified for kinetically activated (athermal or nonequilibrium) material transformations in the HAZ, such as martensite formation in hardenable steels, structural embrittlement of various alloys and austenite stabilization in Hadfield steels (Ref. 2). Finally, temperature gradients are used to characterize the tendency for weld distortion or residual stresses leading to thermal cracking, especially in materials of low heat dissipation such as stainless steels, and hot-short metals (Ref. 4).

For a certain material, solidus and liquidus isotherm data are drawn from the phase diagram and cooling cycle data from the continuous cooling transformation (CCT) diagrams — Fig. 8 for stainless steel 304 (Ref. 22) — while proper temperature gradients are determined from tables of material properties (Ref. 23). If heat transfer in scan welding is temporarily ignored, the first step in the design of the desired thermal field $\underline{T}_d$ involves construction of the material constitutive temperature distribution $\underline{T}_m$ using the above data. Figure 9 illustrates the development of the transverse profile of $\underline{T}_m$ from the specified widths of the molten zone w_s (solidus temperature isotherm T_s), annealing region w_{h1} (isotherm T_{h1}) and transformation (e.g., sensitization) area w_{h2} (isotherm T_{h2}), as

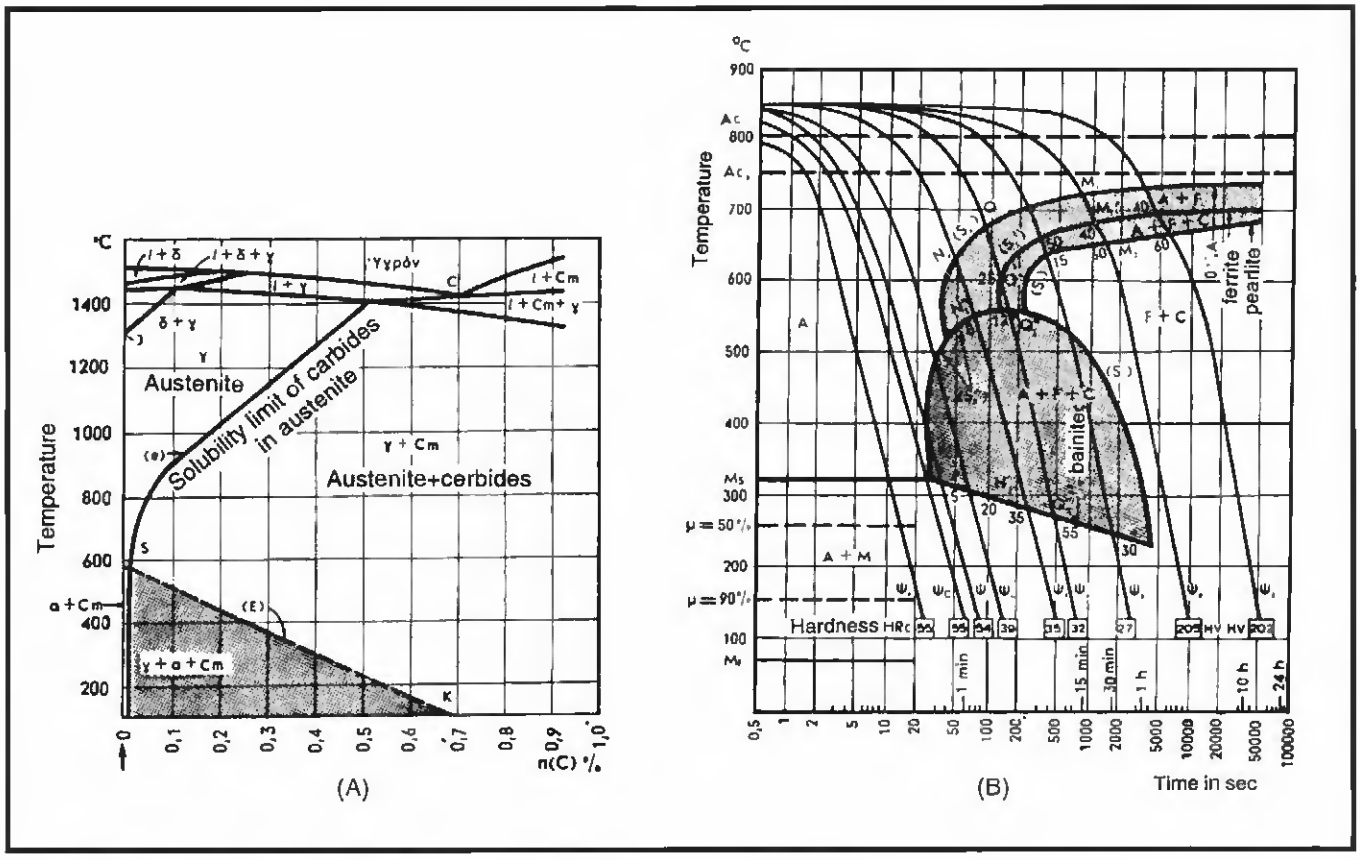

Fig. 8 — Phase diagram and CCT diagram for stainless steel 304.

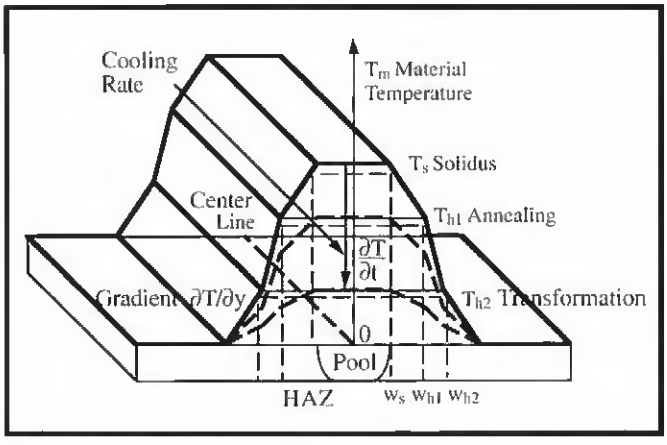

Fig. 9 — Specification of constitutive material temperature field T_m.

well as a constant temperature gradient $\partial T/\partial y$ in the surrounding material. This profile is uniformly extruded along the centerline direction to yield the 3-D distribution $\underline{T}_m(t)$, deflated with time to room temperature at a constant cooling rate $\partial T/\partial t$. This material constitutive field $\underline{T}_m$ represents a fictitious distribution, to which the eventual reference field $\underline{T}_d$ must approach as much compatibility as the welding heat transfer allows. That is, in addition to the material information in $\underline{T}_m$, the desired temperature $\underline{T}_d$ should also incorporate the welding conduction dynamics, *e.g.*, described by the linearized analytical model of Equation 4. Thus, an optimal approximation of $\underline{T}_m$ by $\underline{T}_d$ can be obtained by minimizing a scalar quadratic function E, representing the temperature errors $\underline{T}_m - \underline{T}_d$ (Ref. 21):

$$E(k) = \frac{1}{2}\left[\underline{T}_m(k) - \underline{T}_d(k)\right]^T\left[\underline{T}_m(k) - \underline{T}_d(k)\right]$$

$$\text{and } \frac{\partial E(k)}{\partial \underline{T}_d(k)} = 0 \Leftarrow \text{solve for } \underline{T}_d(k). \quad (7)$$

The resulting optimal reference conditions $\underline{T}_d$, $\underline{Q}_d$ provide a starting point for further improvement of the specification $\underline{T}_d$ using the numerical simulation (Equations 1–3). This allows for more flexibility and realistic rendering of nonlinear thermal effects in scan welding. These include the arbitrary geometry of the part shape and weld centerline (*e.g.*, a fillet weld or with filler material addition), temperature dependence of material properties with latent thermal effects, metallurgical transformations of the weld material, surface effects such as radiation, inert gas convection and conduction to the fixtures, as well as the power intensity distribution of the heat source. Thus, the reference field $\underline{T}_d$ is stipulated through an off-line parametric optimization of the process conditions using the computer simulation above. Alternatively, the desired $\underline{T}_d$ can be designated directly through experimental measurement on the weld surface during an optimal off-line pilot welding test in the laboratory. In this reference test, the temperature hill is recorded by the infrared camera in order to be specified as $\underline{T}_d$ and reproduced subsequently by the thermal controller in real-time processing. Since the latter takes place under the same experimental conditions as the pilot test, no calibration of the measured infrared

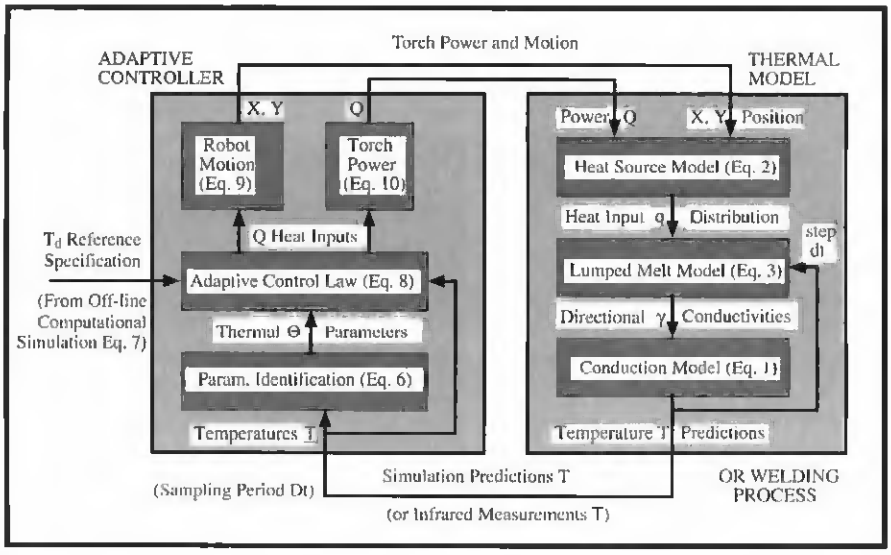

Fig. 10 — Flow diagrams of the thermal model and adaptive controller and their feedback interconnection.

emission field for temperature or size is necessary.

Adaptive Control

As illustrated in Fig. 1, the feedback control scheme uses in-process temperature measurements $\underline{T}$ to determine the heat input distribution $\underline{Q}$ that is required to obtain the specified thermal distribution $\underline{T}_d$ (Fig. 9) repetitively in discrete time. A closed-loop regulation algorithm is necessary to compensate for process disturbances in the ambient heat transfer and the heat source performance for certain welding parameter alterations such as thermal drift of the material properties and for transient effects at the start and end of the operation (arc spatter, molten craters, etc.). Such an adaptive control scheme has been adapted from the original multivariable algorithm in Ref. 24. In this thermal regulation strategy, if the sampling period Dt is long enough to cover the measurement, computation and process delays in each discrete-time control iteration, the MIMO linearized ARMA model of Equation 4 can be inverted to form the basis of a stable one-step adaptive control law. With the specified temperature values $\underline{T}_d(k+1)$ in place of the anticipated $\underline{T}(k+1)$, and with the feedback thermal measurements $\underline{T}$ in place of the temperature data $\underline{T}(k) \ldots \underline{T}(k-n)$ in the augmented vector $\underline{S}(k)$, as well as the applied past input values $\underline{Q}(k-1) \ldots \underline{Q}(k-n)$, Equation 4 can be solved for the necessary heat inputs $\underline{Q}(k)$ in $\underline{S}(k)$:

$$\underline{T}_d(k+1) = \Theta(k) \cdot \underline{S}(k) \Leftarrow \text{solve for } \underline{Q}(k). \qquad (8)$$

The resulting heat input distribution $Q(i; k)$ could, in principle, be induced directly at each pixel element of the part surface in raster-scanned welding by a rapidly deflected laser or electron beam, as already mentioned. However, in vector-scanned welding by a mechanically driven, concentrated torch, this heat flux surface as shown in Fig. 7 must be implemented by properly guided sweeping and scaling of the localized power density distribution of the heat source, manipulated through the torch trajectory $X(k)$, $Y(k)$ and intensity $Q(k)$ — Fig. 1. As it appears in the last term of Equation 2, the point heat source introduces a radially symmetric Gaussian thermal distribution q at its current location, which can generate the required heat input $Q(i; k)$ by spatial and temporal superposition as the torch moves. An efficient strategy for this torch guidance is to locate the heat source at each time k at the location i with the maximum heat input requirement $Q(i; k)$, *i.e.*, at the point of greatest thermal demand. By tracing the locus of the maximum of the Q distribution, the torch is continuously driven to follow the region where its thermal actuation is needed most:

$$X(k) = \text{int}\left[(i-1)/m\right] \cdot Ds,$$
$$Y(k) = \text{mod}\left[(i-1)/m\right] \cdot Ds$$
$$\text{for } \max\left[Q(i; k)\right] \qquad (9)$$

where m is the grid width ($m = 5$ in Fig. 7). In the same way, the torch power $Q(k)$ is modulated proportionally to the maximum value of the Q distribution on which it is located:

$$Q(k) = K \cdot \max\left[Q(i; k)\right] \cdot Ds^2 \quad (10)$$

with K being the power gain. Equations 9 and 10 define the control law of the torch motion to point $X(k)$, $Y(k)$ and torch power $Q(k)$ during the k-th sampling period Dt. Implementation of this heat source transition in the laboratory setup by a servosystem or robot, as shown in Fig. 3, ensures a smooth torch trajectory between its two successive locations, consisting of a straight, constant-velocity segment with parabolic blends at its ends, due to the acceleration and deceleration of its motion. Finally, the heat source power $Q(k)$ follows a rapid first-order (exponential) transient to its final value during the sampling period Dt, because of the fast dynamics of the welding transformer. Figure 10 shows a flow chart of this adaptive control algorithm with thermal parameter identification, as well as its input-output interaction to the numerical simulation model.

Results and Discussion

The above thermal regulation strategy has been implemented in scan welding using both off-line computation, with the simulation software in place of the process hardware (Fig. 10), and real-time experimentation on the plasma-arc laboratory setup, with feedback of infrared thermal images to the control computer, under identical conditions. The scan welding tests involve autogenous, bead-on-plate processing of the stainless steel coupon of Fig. 7 along a composite weld centerline, consisting of three segments as shown in Fig. 11, with process parameters similar to the open-loop configuration. The desired dynamic reference field $\underline{T}_d(t)$ is specified so as to ensure a longitudinally uniform thermal distribution, with a smooth normal temperature profile across the weld bead (Fig. 11A) and with a uniform exponential rise in time from the ambient to the final thermal conditions. This nominal distribution $\underline{T}_d$ was developed through numerical simulation, by a constant, uniform line heat source along the weld centerline segments of the z-pattern, with power density at 30 kW/m.

In the computational model, the grid resolution is $ds = 1$ mm for the large grid and the time increment $dt = 0.05$ s. For the stainless steel coupons (304), the thermal diffusivity is $\alpha = 0.38 \cdot 10^{-5}$ m^2/s for the solid and $\alpha' = 1.32 \cdot 10^{-5}$ m^2/s for the melt, the conductivity averages $\lambda = 27.7$ W/mK, the density $\rho = 7.1 \cdot 10^3$

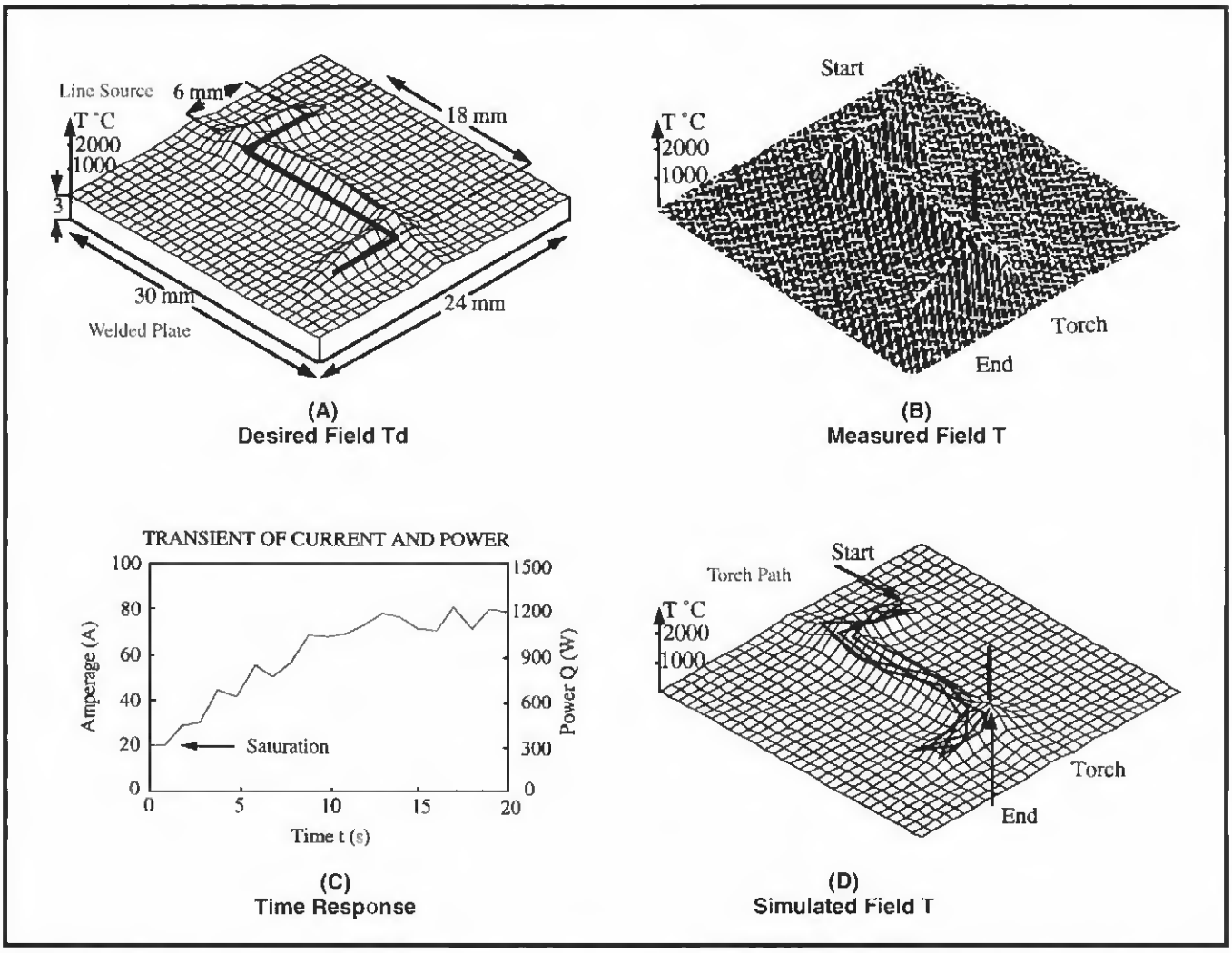

Fig. 11 — Closed-loop thermal control tests of scan welding. A — Desired temperature field T_d (simulation); B — experimental infrared temperature hill T; C — time response of torch heat input Q(k); D — simulated temperature hill T with torch path.

kg/m³, and the latent heat of fusion H = 274 kJ/kg. The ambient temperature is T_a = 20°C (68°F), the heat transfer coefficient 70 W/m²K, and the weld surface emissivity ε = 0.79, determined using comparative contact measurements by K-type thermocouples. The PAW torch characteristics, *i.e.*, its efficiency f = 0.71 and distribution radius s = 1.2 mm, are calibrated by comparison of the simulated solidus T_s isotherm dimensions to the size of the weld nugget section. The torch power is limited by saturation to the amperage range 20–120 A, and the manipulator motion is constrained within the coupon area, when it is occasionally commanded to a location off the weld edges. The torch elevation is kept constant at 3 mm above the weld surface. Welding starts at one end of the *z*-pattern (Start), and is shown in Fig. 11 with the torch on one of its corners (End). The computer regulation routine implements the control laws of Equations 9 and 10 for the torch motion $X(k)$, $Y(k)$ and power $Q(k)$, respectively, on the basis of the multivariable algorithm of Equation 8. The parameters $\Theta(k)$ in this linearized formulation are updated by the adaptation law of Equation 6 from their initial estimates, obtained by unit thermal perturbations of the numerical simulation at the initial conditions $Q_d = 0$, $T_d = T_a$, as already explained. The control gain is empirically determined to K = 23.5, and the sampling period of the control iterations is set to Dt = 1 s.

Figure 11B illustrates the eventual temperature hill $\underline{T}$ on the top surface of the scan welded coupon after t = 20 s, as measured by the infrared pyrometer, while Fig. 11C shows the respective prediction of the thermal field $\underline{T}$ by computer simulation. As shown in the open-loop tests of Fig. 4, their comparison validates the utility of the numerical model as an off-line computational test bed for the development of real-time thermal control systems in scan welding. The RMS temperature deviation of the experimental from the simulated field is 28 K, while its respective error with respect to the reference distribution $\underline{T}_d$ is 61 K. This larger thermal deviation of the actual from the desired temperature field is attributed to speed limitations of the closed-loop system due to the prolonged sampling period Dt, which is needed to provide for the time-consuming multiple temperature measurements at the weld surface nodes. Despite the bandwidth constraints of the infrared sensor, the feasibility of successful regulation of the two-dimensional thermal distribution in scan welding by the previous control strategy is demonstrated in Fig. 11. As shown in the off-line experiments in Fig. 4, the deviations of the thermal hill $\underline{T}$ from $\underline{T}_d$ are only significant at the torch loca-

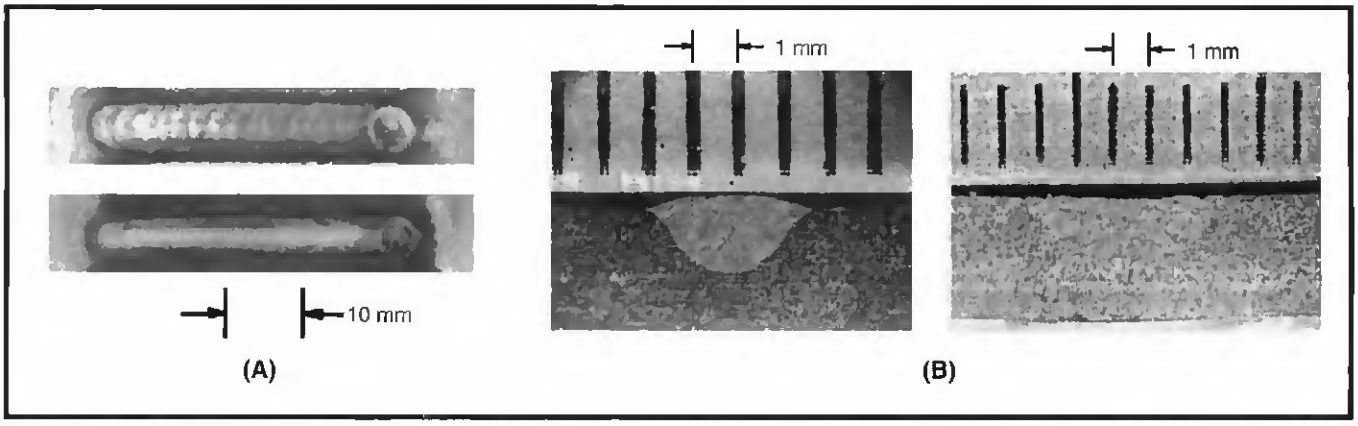

Fig. 12 — Comparison of a traditional plasma-arc weld (A, left, at 80 A, speed 2 mm/s) and a scan bead-on-plate weld (B, right, 80 A and reciprocation 2 Hz). A — Top side bead macrographs (actual size); B — transverse sections of the weld nugget (9X).

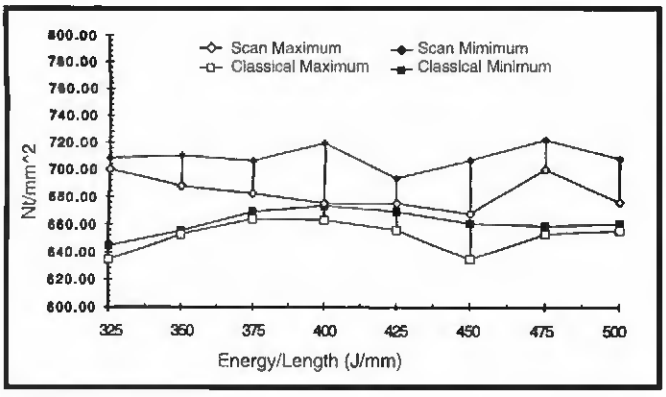

Fig. 13 — Static fracture loads across classical and scan weldments, fabricated at equivalent energy/bead length conditions (ten welds of each type tested at each rating).

tion because of plasma-arc effects, as well as at the ends of the weld bead on the coupon edges because of uncertainties in the assumed heat transfer conditions to the environment. The measured steady-state temperature T along the z-pattern exceeds the solidus temperature $T_s = 1400°C$ (2552°F) of the material, resulting in a continuous molten zone along the joint.

The computed path of the heat source during this closed-loop test is also shown in Fig. 11C and consists of a zig-zag line defined by the successive torch locations $X(k)$, $Y(k)$, within a band of width about ±3 mm along the weld centerline. As expected, this jagged torch trajectory attempts to track the moving peak of the thermal distribution Q in real time, *i.e.*, the weld region with the highest heat input demand. For example, as the torch operates near one of the weld centerline ends, the other end finds the time to cool down yielding a larger deviation from the reference field, and thus the controller directs the heat source toward that end. This results in a continuous reciprocation of the torch along the weld joint, in conformity to the scan welding motion. The respective time response of the applied heat source power $Q(k)$ is depicted in Fig. 11D. It appears that this transient of the current follows the exponential evolution of the specified thermal reference T_{cl}, while its noise peaks can be correlated to the crooked torch trajectory.

This distribution and dynamics of the temperature field in computer-controlled scan welding gives rise to peculiar thermal characteristics of the joint relative to traditional welds. Figures 4 and 11 illustrate the different features of the two arrangements. In traditional welding, the concentrated temperature hill results in a localized ellipsoidal weld pool, which melts the base material at its front part and solidifies at its back part in the longitudinal direction of the joint as it proceeds along with the torch motion. Thus, in classical serial welding, the sequential torch motion produces the weld bead in progressive longitudinal steps as the torch moves. In scan welding, the longitudinal uniformity of the temperature hill along the weld direction yields an elongated pool covering the full length of the joint, and growing and solidifying in the cross-sectional (transverse) directions (*i.e.*, in the direction of the heat flow). This is because the fast torch reciprocation generates an almost uniform line heat source distribution along the joint, yielding a two-dimensional heat transfer across the weld centerline. Thus, the torch reciprocation in scan welding deposits the entire weld bead length simultaneously, in gradual cross-sectional increments. As a result, scan welds do not display the familiar ripples on the bead surface, and can also reduce craters and strikes where the arc is initiated since this position is then overlapped by torch reciprocation. As already mentioned, these defects are a major cause of failures (Ref. 4). Figure 12A shows the top side macrographs of a conventional and a scanned weld bead made by open-loop bead-on-plate PAW on stainless steel at equivalent thermal conditions, as shown in Fig. 4.

This difference in the liquid-solid interface geometry and the dissimilar thermal boundary conditions from the heat source in the two methods result in different melt circulation regimes in the pool. In conventional welding, the steady-state geometrical configuration of the pool following the torch motion yields at equilibrium a fully developed, constant, 3-D flow field with intense convective heat transfer and rapid melting and freezing of the metal at the leading and trailing interface fronts, respectively. This vigorous circulation of the melt results in accelerated thermal convection and solidification in the mushy zone (Ref. 3). On the other hand, in scan welding the distributed heat input produces a considerably decelerated heat flow. The elongated pool with changing cross-sectional geometry results in a transient 2-D circulation, agitated periodically at each torch pass and causing fusion and solidification in progressive steps at the lateral weld interface. This results in controlled melt freezing and development of the scan weld bead. The solidification rate of scan welds is not dependent on the travel speed of the torch as in classical joints,

but can be separately controlled by the diminishing source power at the end of welding. Thus, cooling of the scanned molten bead can be specified as needed for the weld microstructure. Figure 12B also compares representative structures at transverse sections of the welds, obtained by the classical and scan welding method under similar heat source conditions as for Fig. 4. In scan welding, the interface between the joint and the base metal is continuous and gradual, as opposed to the clear solid boundary that separates these two regions in traditional welding. Figure 13 presents the results of static tensile strength tests of traditional and scan weldments (ASTM Standard A 370-92) perpendicular to the joint on a universal testing machine. This figure compares the fracture load ranges for classical and scan welds fabricated at equivalent conditions of energy-per-unit length of the joint (Ref. 10).

Conclusions

In summary, the previous discussion revealed the potential of introducing automation hardware technology, as well as control software methodology, for the redesign of traditional sequential methods to scan welding techniques. In particular, a numerical simulation of the temperature and solid-liquid phase distribution was developed for scan welding, consisting of a finite-difference conduction formulation, an embedded lumped melt flow model and a heat source description. This computational model was validated against infrared temperature measurements on the top surface of stainless steel scan weldments. The simulation served for the establishment of a linearized multivariable model of the heat transfer in the weld, and for the off-line estimation of its thermal parameters, which are updated in real time through infrared data by a least-squares identification technique. The same thermal simulation was also used to develop a desired reference temperature distribution on the basis of specified isotherm, cooling cycle and temperature gradient data to ensure a desirable material structure. This specification was used in the linearized thermal model to establish an adaptive control strategy for regulation of the torch power and guidance of its motion to the area of highest thermal demand. This was implemented both computationally and on a robotic PAW station in the laboratory, and yielded a reciprocating torch trajectory and almost uniform thermal distribution along the weld centerline, as expected from a scan welding technique.

Implementation of scan welding is presently limited to autogenous welding processes, while hybrid techniques, involving a nonautogenous source with material transfer along the joint only, together with an autogenous scanned heating source, are currently explored. Also, scan welding with a mechanically guided torch is best applicable to relatively short and smooth joint paths, depending on the dynamic characteristics of the positioning table or robot. For longer or jagged joint designs, scanning can be implemented in a piece-wise manner on separate consecutive segments of the weld. Alternatively, a high-bandwidth beam source (laser, electron) may be employed to ensure a scanning motion considerably faster than the thermal dynamics of the weldment, depending on the part material, size and heat transfer conditions. In scan welding, the heat source can be operated steadily at its maximum or optimal power rating throughout its motion, since the scanning speed is adjusted accordingly by the thermally regulated setup. Also, automated realization of any desired thermal distribution leads to incorporation of auxiliary stages to the main welding operation, *i.e.*, preheating and postheating steps, since these can be conveniently implemented in process by the thermally controlled scanning system. These features make temperature control in scan welding suitable to thermally-sensitive materials, in which the temperature distribution and cycles must be closely regulated. This application of scan welding to a variety of welded materials and joint designs and the resulting structural and mechanical properties of the weldments is presently under investigation.

Acknowledgment

This research is supported by NSF Grant DMI-9553038.

References

1. Hardt, D. E. 1990. Real-time process control: Limits to progress. *ASME Manufacturing Review* Dec., pp. 40–46.

2. Linnert, G. E. 1968. *High Alloy Steels Fundamentals*. ASM International, Metals Engineering Institute, Materials Park, Ohio.

3. Hayden, H. W., Moffatt, W. G., and Wulff, J. 1965. *The Structure and Properties of Materials*. Vol. III, Mechanical Behavior. New York, N.Y., J. Wiley and Sons.

4. Masubuchi, K. 1980. *Analysis of Design and Fabrication of Welded Structures*, New York, N.Y., Pergamon Press.

5. Miyachi, H. 1989. In-process control of root-gap changes during butt welding. Ph.D. thesis. Dept. of Mechanical Engineering, MIT, Cambridge, Mass.

6. Kannatey-Asibu, E. 1989. Split-beam laser welding. *Trends in Welding Research*. ASM International, Gatlinburg, Tenn., pp. 443–451.

7. Doumanidis, C. C. 1995. Thermal regulation of material transformations in multiple-source arc welding. *Welding Journal* 74(6): 185-s to 196-s.

8. Doumanidis, C. C. 1996. *Scan Welding Method and Apparatus*. U.S. Patent No. 5,552,575. Tufts University, Medford, Mass.

9. Lukens, W. E., and Morris, R. A. 1982. Infrared temperature sensing of cooling rates for arc welding control. *Welding Journal* 61(6): 27–39.

10. Doumanidis, C. C. 1993. Scan welding: A new distributed thermal process. *Proceedings of the Intl. Conf. on Modeling and Control of Joining Processes*, Orlando, Fla., pp. 273–280.

11. Paschkis, V. 1943. Establishment of cooling curves of welds by means of electrical analogy. *Welding Journal* 22(10): 462-s to 483-s.

12. Cristensen, N., Davies, V. L., and Gjermundsen, K. 1965. The distributions of temperatures in arc welding. *British Welding Journal* 12(2): 54–75.

13. Thorn, K., Feenstra, M., Young, J. C., Lawson, W. H. S., and Kerr, H. W. 1982. The interaction of process variables. *Metal Construction* 14(3): 128–133.

14. Rosenthal, D. 1941. Mathematical theory of heat distribution during welding and cutting. *Welding Journal* 20(5): 220-s to 234-s.

15. Tsai, C. L. 1988. Modeling of thermal behaviours of metals during welding. *Trends in Welding Research in the U.S.* ASM, Materials Park, Ohio, pp. 77–89.

16. Hibbitt, H. D., and Marcal, P. V. 1973. A numerical thermomechanical model for the welding and subsequent loading of a fabricated structure. *Computers and Structures* 3(5): 1145–1174.

17. Karlsson, L., and Lindgren, L. E. 1991. Combined Heat and Stress-Strain Calculations. *Modeling of Welding, Casting and Advanced Solidification Processes V*. TMS, pp. 187–202.

18. Marquis, B. P., and Doumanidis. C. C. 1993. Distributed-parameter simulation of the scan welding process. *Proceedings of the Intl. Conference on Modelling and Simulation*. IASTED, Pittsburgh, PA. pp. 146–149.

19. Giedt, W. H., Wei, X. C., and Wei, C. R. 1984. Effect of surface convection on stationary GTA weld zone temperatures. *Welding Journal* 63(12): 376-s to 383-s.

20. Tzafestas, S. G. 1982. *Distributed Parameter Control Systems*. Oxford, U.K., Pergamon Press.

21. Astrom, K. J., and Wittenmark, B. 1995. *Adaptive Control*. Reading, Mass, Addison-Wesley.

22. Konofagos, K. 1973. *Industrial Alloys*. Vol. III, Physical Metallurgy. Athens, Greece.

23. McClintock, F. A., and Argon, A. S. 1966. *Mechanical Behavior of Materials*. Reading, Mass., Addison-Wesley.

24. Goodwin, G. C., Ramadge, P. J., and Caines, P. E. 1980. Discrete-time multivariable adaptive control. *IEEE Trans. on Automatic Control* 25(3): 449–456.

Correction

In the September 1998 *Welding Journal*, "Assessment of Numerical Procedures for Residual Stress Analysis of Multipass Welds" by J. K. Hong, C. L. Tsai and P. Dong (pages 372-s to 382-s) contained some incorrect figures. The *Welding Journal* apologizes for the errors. Corrected figures follow.

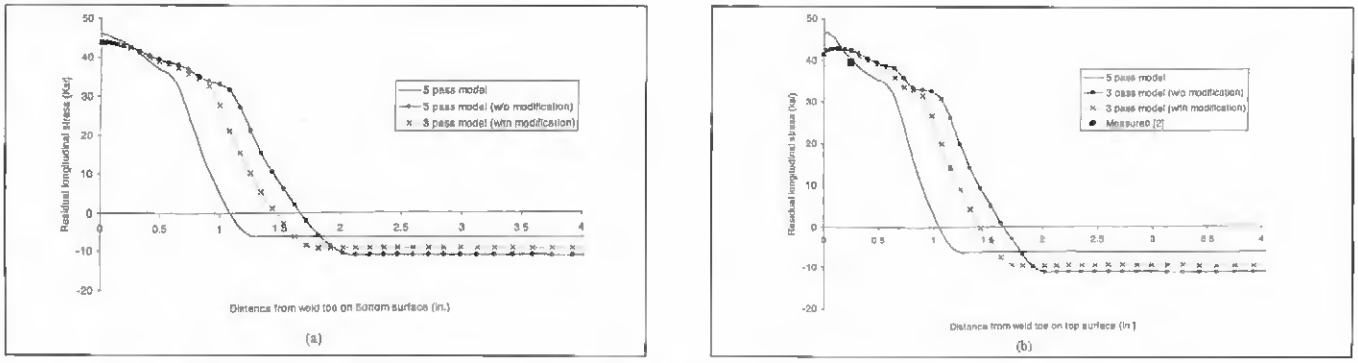

Fig. 9 — Residual longitudinal stress distributions for a plate model: A — On bottom surface; B — on top surface.

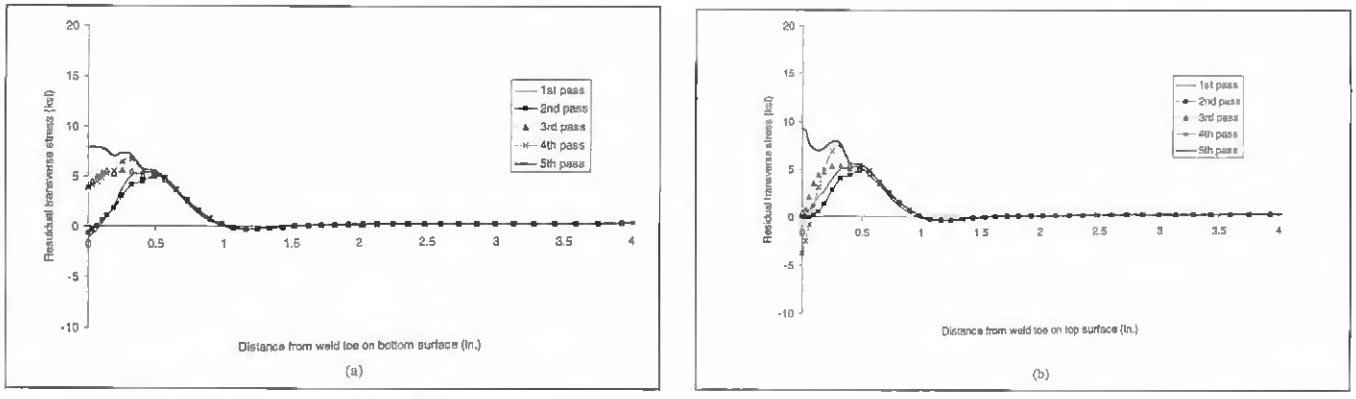

Fig. 11 — Residual transverse stress distributions after immediate passes for a plate model: A — On bottom surface; B — on top surface.

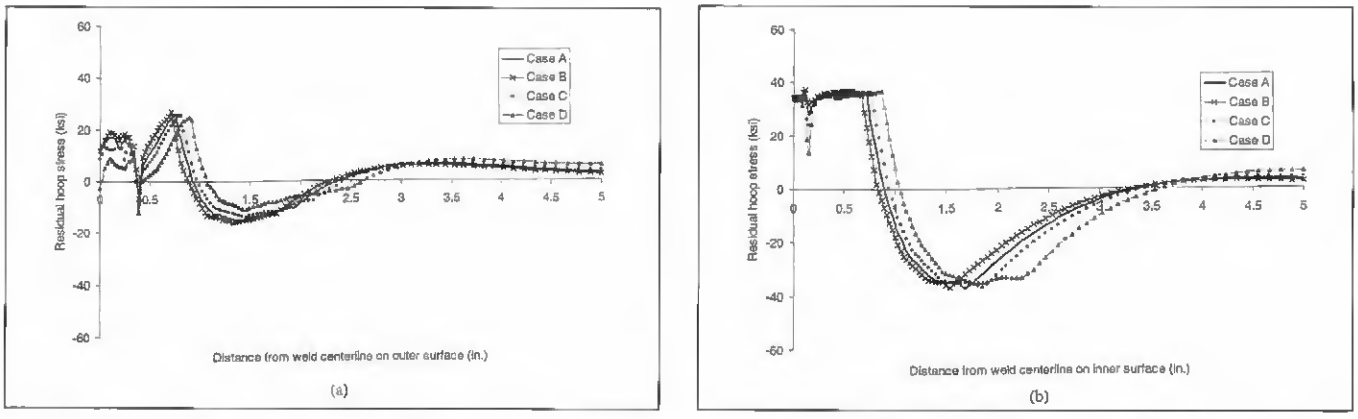

Fig. 19 — Residual hoop stresses for different heat input magnitudes for a pipe model (prescribed initial temperature for weld metal is room temperature): A — On outer surface; B — on inner surface.

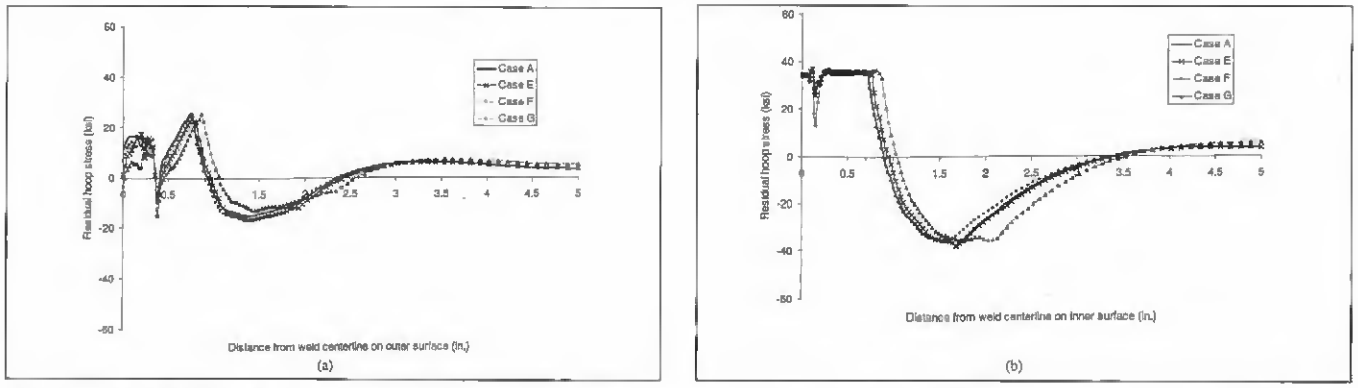

Fig. 21 — Residual hoop stresses for different heat input magnitudes for a pipe model (prescribed initial temperature for weld metal is melting temperature): A — On outer surface; B — on inner surface.